PAPER

Check for updates

Effect of seed layer thickness on the Ta crystalline phase and spin Hall angle†

K. Sriram, [ID] ‡[a] Jay Pala,‡[a] Bibekananda Paikaray,[a] Arabinda Haldar[b] and Chandrasekhar Murapaka*[a]

Heavy metal–ferromagnet bilayer structures have attracted great research interest for charge-to-spin inter-conversion. In this work, we investigated the effect of the permalloy (Py) seed layer on the tantalum (Ta) polycrystalline phase and its spin Hall angle. Interestingly, for the same deposition rates the crystalline phase of Ta deposited on the Py seed layer strongly depends on the thickness of the seed layer. We observed a phase transition from α-Ta to (α + β)-Ta while increasing the Py seed layer thickness. The observed phase transition is attributed to the strain at the interface between the Py and Ta layers. Ferromagnetic resonance-based spin pumping studies reveal that the spin-mixing conductance in the (α + β)-Ta is relatively higher as compared to the α-Ta. Spin Hall angles of α-Ta and (α + β)-Ta are obtained from the inverse spin Hall effect (ISHE) measurements. The spin Hall angle of (α + β)-Ta is estimated to be $\theta_{SH} = -0.15 \pm 0.009$ which is relatively higher than that of the α-Ta. Our systematic results connecting the phase of Ta with the seed layer and its effect on the efficiency of spin to charge conversion might resolve ambiguities across various literature and open up new functionalities based on the growth process for emerging spintronic devices.

1. Introduction

Rapid developments in the field of spin to charge conversion and *vice versa* allow for the electrical control of spin-based phenomena – an essential requirement to integrate spintronic devices with the existing microelectronics platform.[1–7] Materials having large spin–orbit coupling (SOC) generate transverse spin current from the longitudinal charge current by the spin Hall effect (SHE) and interfacial Rashba–Edelstein effect (REE). SHE and REE are responsible for the conversion of the charge current into a spin current in heavy metals (HM). The efficiency of charge-to-spin interconversion can be quantified by a parameter called spin Hall angle (θ_{SH}).[8–12] The inverse effect is known as the inverse spin Hall effect (ISHE) that converts the spin current to a charge current and is found to be the most promising technique for the electrical detection of spin currents.[13,14] One of the key ingredients of the ISHE for converting the spin current to a charge current is a large SOC thus, heavy metals, such as Ta, W, Pt and Pd are the

natural choice.[15] In a typical spin to charge converter, a heavy metal (HM)/ferromagnet (FM) interface is used where the spin currents are injected into the HM layer from the FM layer through spin pumping.[16–19] According to Tserkovnyak *et al.*,[20] time-dependent magnetization transfers angular momentum from the FM to the FM/HM interface *via* coupling of the local magnetic moments of the FM with the conduction electrons of the HM. This loss of angular momentum in the Ta layer enhances the ferromagnetic resonance (FMR) linewidth which is an additional damping ($\Delta\alpha$) that arises due to the spin pumping to the bulk damping (α_{FM}) of the FM. In the spin pumping mechanism, oscillating magnetization at the FM/HM interface induces a spin imbalance in the HM layer thereby generating a spin current in the HM. Effective spin-mixing conductance ($g_{\uparrow\downarrow}$) is a key parameter in quantifying the efficiency of spin pumping which is a measure of spin current injection from the FM to the adjacent HM sink. In spin to charge conversion, $g_{\uparrow\downarrow}$ is an interfacial parameter, which can be influenced by interfacial texture, morphology and the crystalline phases of HMs.[21–27] Among the choices of HMs, Ta is one of the most studied materials in the FM/HM system due to its observed relatively large $g_{\uparrow\downarrow}$ and spin Hall angle (θ_{SH}).[28,29] Ta is found to possess two different crystalline phases known as the stable α-phase and metastable β-phase which are associated with having cubic and tetragonal structures, respectively. In the recent past, extensive research has been carried out on the value of the θ_{SH} for the different phases of Ta and a variety of values have been reported for the θ_{SH} which are as follows:

[a]Department of Materials Science and Metallurgical Engineering, Indian Institute of Technology Hyderabad, Kandi-502284, Telangana, India.
E-mail: mchandrasekhar@msme.iith.ac.in
[b]Department of Physics, Indian Institute of Technology Hyderabad, Kandi-502284, Telangana, India

†Electronic supplementary information (ESI) available: Permalloy optimization and thickness dependent GIXRD. See DOI: 10.1039/d1nr06007d
‡These authors have equally contributed to this work.

$\theta_{SH} = -0.10$ for amorphous Ta,[30] $\theta_{SH} = -0.15$ for α-Ta,[31] $\theta_{SH} = -0.16$ for $(\alpha + \beta)$-Ta,[32] and $\theta_{SH} = -0.10$ to -0.25 for β-Ta.[33] However, the reported large value is in a high resistive phase that hinders the realization of low power SOT devices. Therefore, there is an immense need for the deposition of low resistive Ta layers. It is clear that the θ_{SH} strongly depends on the crystalline phase of Ta which led to several investigations on the structure of Ta interfaced with different FMs.[12,34] However, structural characterizations are focused only on a bare Ta film in most of these studies and the detailed investigations on the effect of a magnetic seed layer on the evolution of the Ta polycrystalline phase are elusive. A direct correlation between the crystalline phase of Ta with the parameters of the $g_{\uparrow\downarrow}$ and θ_{SH} is critically important to addressing a wide variety of results obtained so far and for the future of ISHE-based spintronic devices.

Here, we report a systematic investigation on the dependence of the Ta polycrystalline phase on the ferromagnetic $Ni_{80}Fe_{20}$ or permalloy (Py) seed layer for different Ta growth rates and thicknesses. Detailed structural characterizations have been conducted in order to identify the phase of Ta using the grazing incidence X-ray diffraction (GIXRD) technique. We reveal the variation of spin pumping properties, $i.e.$, the magnitude of $g_{\uparrow\downarrow}$ as a function of various Ta phases using broadband ferromagnetic resonance (FMR) spectroscopy. Furthermore, we have estimated the spin to charge conversion efficiency parameter, the θ_{SH} for various Ta phases obtained from different Py thicknesses using ISHE measurements. Our results correlate critical parameters, the $g_{\uparrow\downarrow}$ and θ_{SH} as a function of the phase of Ta. Our results also open up a potential route for tuning the crystalline phase and the SOC of a heavy metal via the seed layer.

2. Experimental methods

Ta thin films were deposited on a naturally oxidized $Si\langle 100 \rangle$ substrate by using the DC magnetron sputtering technique. The base pressure of the chamber was always kept below 3×10^{-7} mbar and a deposition pressure of $\simeq 5 \times 10^{-3}$ mbar was maintained during the deposition. Prior to any sample deposition, pre-sputtering of the targets was carried out for 2 min with the shutter closed. We deposited the following series of thin films; series A: Si/Ta (50 & 18 nm) at different deposition rates $(D_R) = 0.08–0.13$ nm s^{-1}, series B: Si/Py (t_{Py})/Ta (18) for $t_{Py} = 4, 8, 12, 16,$ and 20 nm, series C: Si/Py (t_{Py}) at 0.10 nm s^{-1}, and series D: Si/Py $(t_{Py} = 20)$/Ta (18) with a Ta deposition rate of $D_R = 0.13$ nm s^{-1}. Note that we only varied the D_R for Ta and the magnetic layer was always deposited at a fixed deposition rate of $D_R = 0.10$ nm s^{-1} in all of our samples. The deposition rate of Ta was tuned by varying the DC power in the range of 60–160 watts during deposition while keeping all other parameters unchanged. The resistivity of Ta and Py was measured by a conventional four-probe method. Structural properties of all of the thin films were determined by the GIXRD technique using Cu-K$_\alpha$ ($\lambda = 1.5406$ Å) as the radiation source. We set the incident angle at $1°$ and performed a 2θ

scan in the range of 20–90° with a scan rate of 0.02° s^{-1}. We used a lock-in based broadband FMR technique to investigate magnetic and magnetization dynamic properties. FMR measurements were carried out in the range of a 4–16 GHz excitation frequency and a 0 to ±300 mT field. ISHE studies were carried out on samples with dimensions of 4 mm × 8 mm. We measured the voltage drop due to the ISHE at the transverse edges of the sample by using Ag paste contacts and all of the measurements were carried out at room temperature.

3. Results and discussion

3.1. Effect of the deposition rates (D_R): Si/Ta (50 & 18 nm)

In order to understand the effect of the deposition rates on the Ta polycrystalline phase, first, bare Ta films, $i.e.$, series A thin films were prepared where the D_R was varied from 0.08 nm s^{-1} to 0.13 nm s^{-1}. GIXRD plots of the Si/Ta (50) thin films for different D_R are shown in Fig. 1(a). High intensity Bragg diffr-
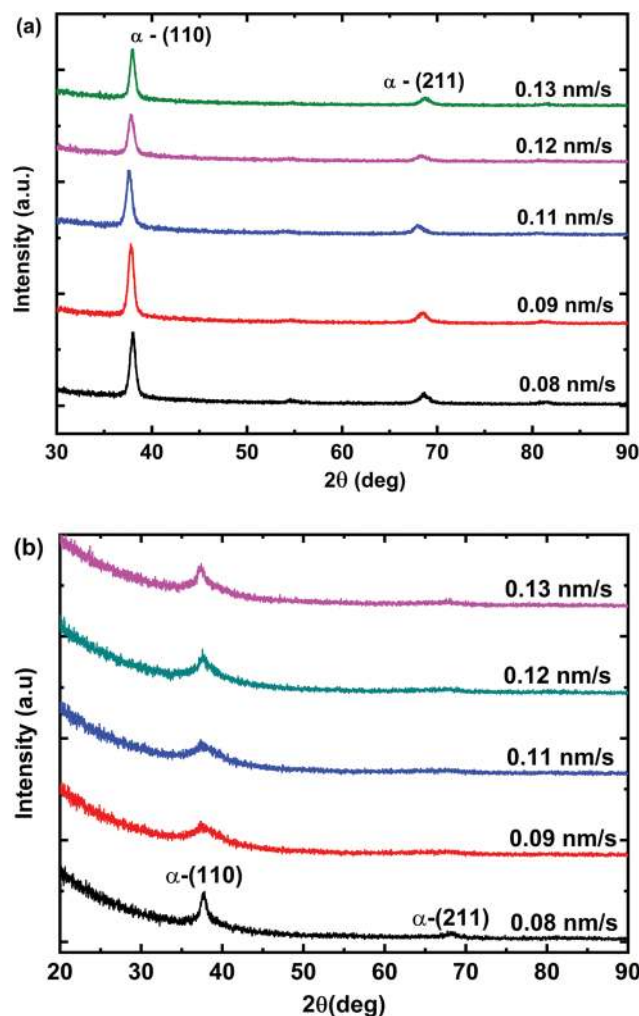

Fig. 1 GIXRD results of Si/Ta (t_{Ta}). (a) 50 nm Ta (b) 18 nm Ta grown at different deposition rates from 0.08 to 0.13 nm s^{-1} showing the single phase α-Ta.

action peaks are observed at $2\theta \sim 38°$ and $2\theta \sim 69.5°$ and the observed 2θ positions correspond to the (110) and (211) planes of the α-phase of Ta, respectively (denoted by α-Ta), which possesses a body-centered cubic (BCC) crystal structure. The calculated interplanar spacing (d) and lattice constant ($a = b = c$) for the BCC-Ta are 2.37 Å and 3.36 Å, respectively. GIXRD results show that the Ta sputtered directly on the Si substrates exhibit nucleation of single phase α-Ta which is in good agreement with previous reports.[35–39] For the bilayer study, we cited the Ta thickness as 18 nm which is higher than the spin diffusion length ($>2\lambda_{sd}$) of Ta which also exhibits the α-Ta phase deposited on Si.

GIXRD results of 18 nm Ta films at different D_R are shown in Fig. 1(b). The GIXRD results of Ta at different D_R reveal that at relatively low deposition rates, atoms have enough relaxation time and diffusivity to occupy energetically favorable atomic positions for the equilibrium state which could be the reason for the formation of the low energy textured (110) plane. By comparing the 50 nm and 18 nm thicknesses of the Ta thin films, there is no significant effect on the Ta phase due to its thickness variations.

3.2. Effect of the seed Py layer: Si/Py (t_{Py})/Ta (18); t_{Py} = 4, 8, 12, 16, 20 nm

To investigate the effect of the seed Py layer thickness on the Ta polycrystalline phase, we examined the sample series B. The GIXRD results of Si/Py (t_{Py})/Ta (18) at $D_R = 0.13$ nm s^{-1} is shown in Fig. 2. One can see the stable α-Ta phase of Ta for t_{Py} = 4 and 8 nm. Interestingly, a phase transition from the α-Ta to (α + β)-Ta was observed for $t_{Py} \geq 12$ nm.

In order to understand the effect of the Py crystalline nature on Ta, we deposited series C: Si/Py (t_{Py}) to investigate the thickness dependent structural behavior in Py films using GIXRD. The GIXRD results are shown in the ESI S1.† The

Fig. 2 GIXRD results of Si/Py (t_{Py})/Ta (18) bilayers for t_{Py} = 4,8,12,16, and 20 nm where Ta deposited at $D_R = 0.13$ nm s^{-1} shows Ta phase transition from α-Ta to (α + β)-Ta phase with a function of seed Py layer thickness.

GIXRD results show that the prominent (111) plane is observed at $2\theta = 44.2°$ in Py layers corresponding to the face-centered-cubic (FCC) crystal structure. The calculated d-spacing and lattice constant for the crystalline phase of Py (t_{Py} = 12, 16 and 20 nm) are 2.04 Å and 3.54 Å, respectively. Interestingly, the observed (111) peak is visible only when the Py thickness is ≥12 nm and no prominent diffraction peak is observed below 12 nm thickness. The promotion of (α + β) phase growth of Ta on crystalline Py ($t_{Py} \geq 12$ nm) could be due to the strain at the interface between the crystalline Py and Ta. To further ascertain the phase transition observed in Ta due to the strain at the interface, we calculated the lattice parameters of the α-Ta phase from both the α-Ta and the (α + β)-Ta deposited on Py of 8 nm and 12 nm thickness, respectively. The lattice constant of α-Ta in Si/Py (12)/Ta (18) was found to be 3.29 Å, which is 3.23% smaller than the lattice constant of α-Ta in Si/Py (8)/Ta (18). This clearly shows the influence of the seed Py layer on the Ta crystalline phase. The strain induced at the interface is causing the nucleation of β-Ta along with α-Ta in Si/Py (12)/Ta (18). Saravanan *et al.*[40] have reported that Ta in contact with crystalline Py generates strain due to lattice mismatch between Ta and crystalline Py. This observation is quite evident as well in our Py/Ta system where strain originates once Py becomes crystallized. The systematic study from Fillon *et al.*[41] on the influence of phase transformation on strain evolution suggests that the strain evolved above critical Py thickness (>8 nm) due to an increase of the lateral volume of the sputtered film after which Py exhibits a crystalline nature. From the above-mentioned studies, it can be noted that the crystalline Py thickness is strongly influencing the Ta phase through strain at the Py/Ta interface. To further confirm the Ta phase transition as a function of the seed Py layer thickness, we deposited and examined series B at different Ta deposition rates from $D_R = 0.08$ to 0.13 nm s^{-1}. Fig. 3(a and b) shows the GIXRD results of the Py (8)/Ta (18) and Py (12)/Ta (18) bilayer structures. The Ta deposited on 8 nm Py always exhibits the α-Ta for the deposition rates chosen in our study. In contrast, Ta deposited on 12 nm crystalline Py shows (α + β)-Ta irrespective of the deposition rates.

This observation from the GIXRD results demonstrates that the Ta crystalline phase is influenced by seed Py thickness irrespective of the Ta deposition rates considered in this work. It is evident that crystalline seed Py promotes the (α + β)-Ta phase by the influence of interfacial strain at the Py/Ta interface. From the above discussion, it can be concluded that the resultant Ta phase is strongly correlated with a seed Py crystalline nature that depends on Py thickness in our study.

3.3. Spin pumping and ISHE for Si/Py (t_{Py})/Ta (18); t_{Py} = 20 nm

To get an insight into the effect of the Ta crystalline phase tuned *via* seed layer thickness on its spin Hall angle, we performed spin pumping studies in Si/Py (t_{Py})/Ta (18) bilayer structures. Therefore, the effect of the Ta phase on the spin Hall angle was systematically investigated. First, we performed FMR measurements on series D [Si/Py (t_{Py} = 20)/Ta (18)]. The derivative of the FMR responses shown in Fig. 4(a) are fitted to
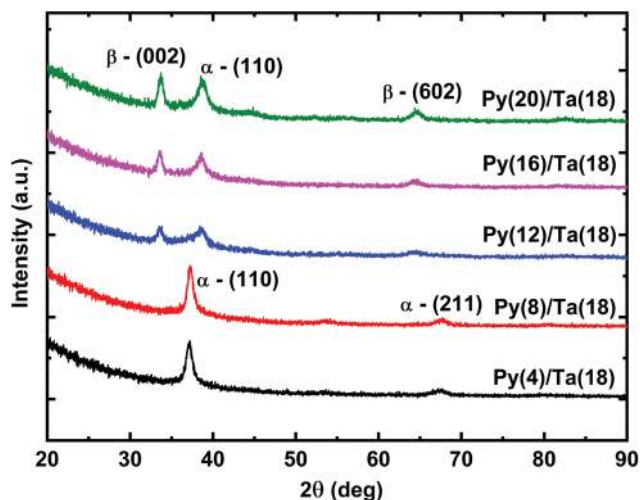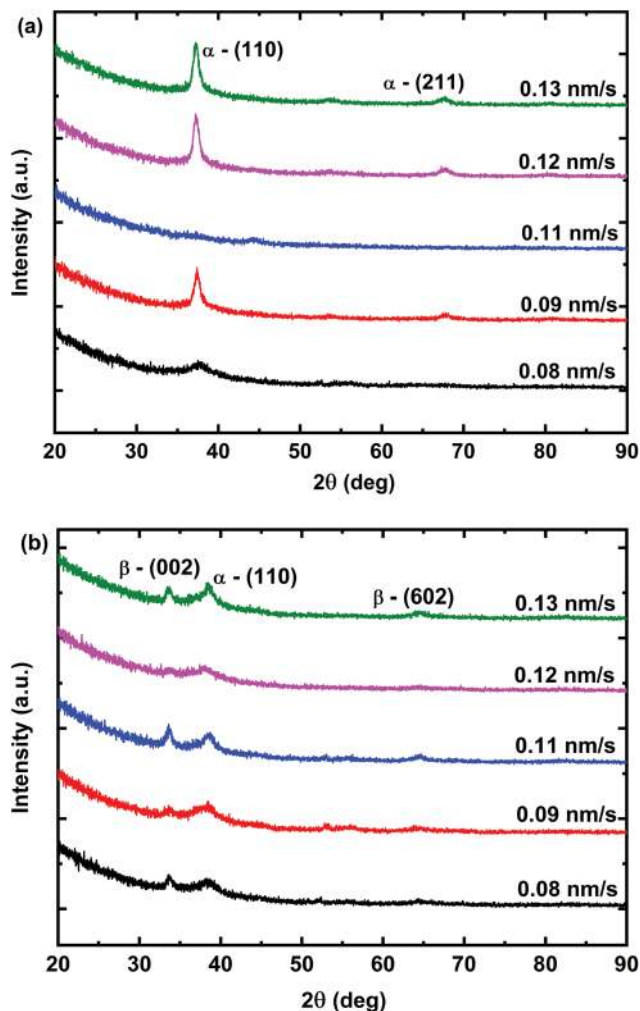
Fig. 3 (a) GIXRD results of Si/Py (8)/Ta (18) bilayer showing α-Ta phase for different Ta deposition rates from 0.08 to 0.13 nm s^{-1}. (b) GIXRD results of Si/Py (12)/Ta (18) bilayer showing ($\alpha + \beta$)-Ta phase for different Ta deposition rates from 0.08 to 0.13 nm s^{-1}.

a derivative Lorentzian function which has symmetric and asymmetric contributions as per the following relation:

$$\frac{dI}{dH} \propto -2K_1 \frac{\Delta H(H - H_r)}{\left[\Delta H^2 + (H - H_r)^2\right]^2} + K_2 \frac{\left[\Delta H^2 - (H - H_r)^2\right]}{\left[\Delta H^2 + (H - H_r)^2\right]^2} \tag{1}$$

where H, ΔH, H_r, K_1, and K_2 are the external field, FMR linewidth (full width at half maximum), resonance field, symmetric and asymmetric amplitudes of FMR signal, respectively.

ΔH and H_r are recorded as fitting parameters from the fit with eqn (1). Fig. 4(b) shows H_r (f) data which are fitted with Kittel's equation:[42]

$$f = \frac{\gamma}{2\pi} \sqrt{(\mu_0(H_r + H_k))(\mu_0 H_r + \mu_0 H_k + \mu_0 M_{eff})} \tag{2}$$

where γ, H_k, μ_0, M_{eff} are the gyromagnetic ratio ($\gamma = 1.85 \times 10^2$ GHz T^{-1}), anisotropy field, vacuum permeability and effective
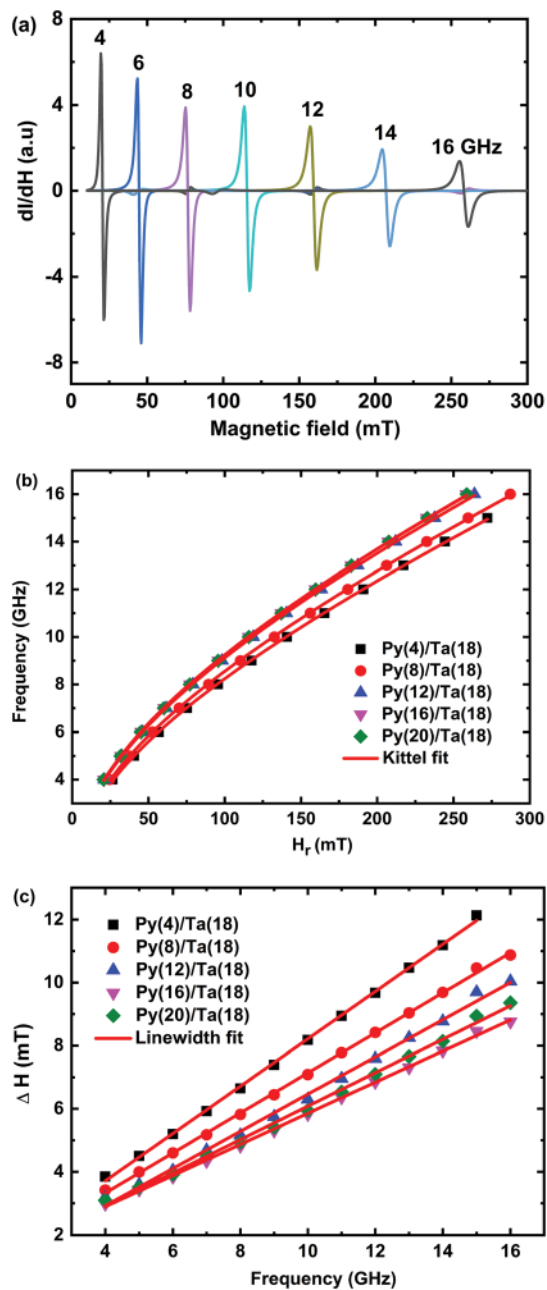

Fig. 4 Ta deposition rate is set to 0.13 nm s^{-1}. (a) Derivative of FMR absorption spectra of Si/Py (20)/Ta (18). (b) Resonance field (H_r) vs. frequency (f) for Si/Py (t_{Py})/Ta (18) where t_{Py} = 4, 8, 12, 16 and 20 nm. (c) FMR linewidth (ΔH) vs. frequency (f) for Si/Py (t_{Py})/Ta (18) where t_{Py} = 4, 8, 12, 16 and 20 nm.

magnetization, respectively. Thus, we obtain M_{eff} and H_k values from the fit with the Kittel equation for all of the samples. Fig. 4(c) shows the FMR linewidth (ΔH) vs. frequency (f) plot and the effective Gilbert damping (α_{eff}) can be determined from the slope using the following expression:

$$\mu_0 \Delta H = \frac{4\pi \alpha_{eff} f}{\gamma} + \mu_0 \Delta H_0 \tag{3}$$

where $\mu_0 \Delta H_0$ is the inhomogeneous linewidth broadening which is related to the magnetic defects or quality of the film. Fit to eqn (3) provides α_{eff} and $\mu_0 \Delta H_0$. The inhomogeneous line width broadening in our samples $\mu_0 \Delta H_0$ is <1 mT.

Additional damping $(\Delta\alpha)$ due to spin pumping can be written as,

$$\Delta\alpha = \alpha_{eff\left(\frac{Py}{Ta}\right)} - \alpha_{(Py)} \qquad (4)$$

where α_{Py} was found to be 0.0066 in our bare Py films. α_{eff} is the direct evidence of spin current induced by spin pumping. The observed α_{eff} for the Py/Ta bilayer is more significant when the Py thickness is <10 nm and decreases at larger Py thicknesses due to large spin accumulation. It suggests that spin pumping is an interfacial phenomenon and the $\Delta\alpha$ caused by spin pumping is proportional to $1/t_{Py}$ which is consistent with earlier reports.[20,32,43–45] Spin pumping induces non-equilibrium spin accumulation that can be estimated from a parameter called effective spin-mixing conductance $(g_{\uparrow\downarrow})$ by using the following expression:

$$g_{\uparrow\downarrow} = \frac{4\pi M_s t_{FM}}{g\mu_o\mu_B}(\alpha_{eff} - \alpha_{Py}) \qquad (5)$$

where g (= 2.1) is the spectral splitting constant, μ_o is the permeability under vacuum, μ_B is the Bohr magnetron, M_s is the saturation magnetization and t_{FM} is the thickness of Py. We calculated the spin-mixing conductance for Si/Py (t_{Py})/Ta (18) bilayers and the maximum value of the $g_{\uparrow\downarrow} = 10.1 \times 10^{18}$ m^{-2} was observed for Si/Py (20)/Ta (18) and the minimum value of the $g_{\uparrow\downarrow} = 7.9 \times 10^{18}$ m^{-2} for Si/Py (8)/Ta (18), which corresponds to the $(\alpha + \beta)$-phase of Ta and the α-phase of Ta, respectively. Spin-mixing conductance $(g_{\uparrow\downarrow})$ is purely an interfacial parameter that quantifies the amount of spin injected from the precessing ferromagnet (FM) to the heavy metal (HM).[18,46–48] E. Šimánek et al.[49] and E. Šimánek.[50] argued that the enhancement of the $g_{\uparrow\downarrow}$ by spin pumping is due to the dynamic electron–electron interaction at the FM/HM interface. A theoretical study of magnetization relaxation by Zwierzycki et al.,[45] confirmed that the $g_{\uparrow\downarrow}$ is due to the coherent scattering of spins within the magnetic exchange length scale. According to Stoner's model discussed by Tserkovnyak et al.,[20,51,52] $g_{\uparrow\downarrow}$ can be correlated with the structural property of the HM since spin transparency (Stoner-enhanced dynamics spin susceptibility) might be dissimilar for different crystal systems. For metallic systems, band structure calculations of the HM give results that are very close to Sharvin conductance (dimensionless conductance means the number of transport channels).[53–55] There could be two reasons for the enhancement of the $g_{\uparrow\downarrow}$ in $(\alpha + \beta)$-Ta. The first reason in our case is the different crystalline phases of the Ta layer that possess different dynamic spin susceptibilities. Due to the mixed phase of Ta, there might be more spin injection due to a greater number of transport channels resulting in large spin-mixing conductance. The second reason is the onset of the (111) plane in Py (12, 16 and 20 nm) which can potentially change the crystal field effect[56] at Py (12)/Ta (18) and also

enhance symmetry breaking.[57] We believe that these are the two major reasons behind the increase of the spin-mixing conductance in the mixed phase than in the single-phase Ta. The variation in the $g_{\uparrow\downarrow}$ is due to the phase fraction of α-Ta and β-Ta. It is worth noting here that the recent works by Bansal et al.[23] and Kumar et al.[32,58] have also reported similar kinds of observations due to the $(\alpha + \beta)$-Ta phase. However, theoretical studies on HM structure dependent spin-mixing conductance are elusive and therefore, it will attract great interest in the community to further *dig* into using first principle studies. Therefore, it is evident that the interface is better transparent in Py/$(\alpha + \beta)$-Ta than in Py/α-Ta for spin injection. In order to investigate the spin-to-charge conversion efficiency, we considered Si/Py (t_{Py})/Ta (18) where t_{Py} = 20 nm, deposited with a Ta deposition rate of 0.13 nm s^{-1}. The derivative FMR signal and ISHE voltage for Si/Py (20)/Ta (18) at f = 9 GHz are shown in Fig. 5(a). We also measured the ISHE voltage for a wide frequency range (4–16 GHz) for Si/Py (20)/Ta (18) with a field
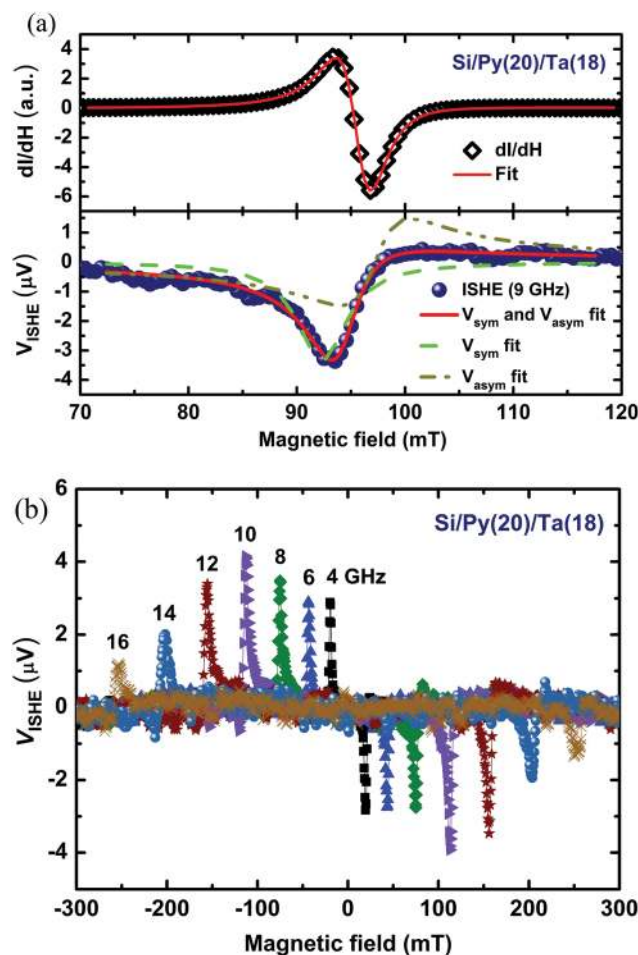

Fig. 5 (a) Ta deposition rate is set to 0.13 nm s^{-1} for Si/Py (20)/Ta (18). Derivative of FMR absorption and corresponding ISHE voltage at 9 GHz excitation frequency with corresponding symmetric and asymmetric fitting. (b). Ta deposition rate is set to 0.13 nm s^{-1} for Si/Py (20)/Ta (18). ISHE voltage as a function of the external field for different GHz frequencies.

sweep of −300 mT to +300 mT as shown in Fig. 5(b). In order to disentangle the voltage contribution from the ISHE among all of the other possible spin rectification effects in our Py/Ta bilayer system, the measured voltage signal was fitted to the Lorentzian equation with a symmetric and an asymmetric contribution,[59–61]

$$V = V_{sym} \frac{(\Delta H)^2}{(H - H_r)^2 + (\Delta H)^2} V_{asym} \frac{2\Delta H(H - H_r)}{(H - H_r)^2 + (\Delta H)^2} \quad (6)$$

where V_{sym} and V_{asym} are the symmetric and asymmetric components of the measured voltage signal. V_{sym} corresponds to the ISHE and V_{asym} has the contributions from the spin rectification effects such as anisotropic magnetoresistance (AMR) and the anomalous Hall effect (AHE).[62] The symmetric and asymmetric contribution fit to eqn (6) is shown in Fig. 5(a). We found that V_{sym} = 3.6 μV which is dominant as compared to V_{asym} = 1.3 μV. Therefore, the major contribution of the observed voltage signal can be attributed to the ISHE. The spin-pumping induced ISHE in our system enables the estimation of the spin current density (J_S) and the θ_{SH} of the Ta layer.

In Py/Ta film, the magnitude of the spin current injected from the Py to the Ta layer can be evaluated from the spin current density formulation,[20] which can be expressed as,

$$|J_S| = \left(\frac{g_{\uparrow\downarrow}\hbar}{8\pi}\right)\left(\frac{\mu_0 h_{rf}\gamma}{\alpha_{eff}}\right)^2 \left[\frac{\mu_0 M_S\gamma + \sqrt{(\mu_0 M_S\gamma)^2 + 16(\pi f)^2}}{(\mu_0 M_S\gamma)^2 + 16(\pi f)^2}\right]\left(\frac{2e}{\hbar}\right) \quad (7)$$

where $\mu_0 h_{rf}$ is the rf magnetic field which is 0.06 mT in our measurements. The spin current density described in eqn (7) is converted into an electromotive force V_{ISHE} due to the ISHE in the Ta layer induced by the spin pumping as per the following relation:[63]

$$V = \left(\frac{1}{\frac{t_{Py}}{\rho_{Py}} + \frac{t_{Ta}}{\rho_{Ta}}}\right) w\, \theta_{SH}\, \lambda_{sd}\, \tan h\left(\frac{t_{Ta}}{2\lambda_{sd}}\right)|J_S| \quad (8)$$

where ρ_{Py} and ρ_{Ta} are the resistivities of the Py and Ta thin films, respectively.[34,50] The parameters w, t_{Ta}, t_{Py} are the width of the signal line (= 200 μm) and the thickness of the Ta and Py layer, respectively. The spin diffusion length (λ_{sd}) is considered to be 3 nm for Ta.[64]

Interestingly, we observed that the Ta thin film with (α + β)-Ta phase shows a higher value for the spin Hall angle, −0.15 ± 0.009, than the α-phase Ta whose θ_{SH} value is = −0.10 ± 0.008. From the observed θ_{SH} values, it is evident that spin to charge conversion efficiency is directly correlated with the phase of Ta and the estimated θ_{SH} values are in good agreement with the reported values.[32] The enlarged spin Hall angle in the Py/Ta phase has low longitudinal resistance due to the presence of a mixed phase where the major contribution comes from extrinsic mechanisms such as skew scattering and side jump scattering as reported by Kumar *et al.*[23,32,58] The crystalline Py can enhance the θ_{SH} by enlarging the interfacial symmetry break-

ing at the Py/Ta interface. Therefore, the key reason for the relatively large θ_{SH} observed in the Py/(α + β)-Ta phase is due to the combined effect of low longitudinal resistance and the enhanced interfacial symmetry breaking. This work presents a promising method for engineering the crystalline phase of Ta *via* seed Py thickness and crystallinity which in turn assist in tuning the spin Hall angle. It also reveals that the effect of thickness and the crystalline nature of the seed ferromagnetic (FM) layer on the crystalline phase of Ta cannot be ignored. It shows that Ta films deposited on a bare Si substrate and FM seed layer can exhibit different crystalline phases hence exhibiting different spin-charge conversion efficiencies. Our systematic investigation on Py/Ta may provide a viable and alternative way to tune the spin conversion efficiency *via* seed layer crystallinity and thickness. Moreover, this study improves the understanding of the seed layer's influence on HM phase transition and the effect of the stack configuration on the performance of SOT based devices.

4.   Summary

The effect of the magnetic seed layer on the phase of Ta has been investigated in detail in the Py/Ta heterostructures. First, the phase of bare Ta films (t_{Ta} = 18, 50 nm) on the Si-substrate has been characterized as a function of deposition rate showing the α-Ta phase for a D_R < 0.2 nm s^{-1} and (α + β)-Ta phase beyond it. The phase of Ta is then systematically studied by depositing it (at D_R = 0.13 nm s^{-1}) on different thickness Py films which were sputtered on the Si-substrate. Si/Py (t_{Py})/Ta (18) bilayers reveal the α-Ta phase for t_{Py} = 4, 8 nm and (α + β)-Ta for $t_{Py} \geq$ 12 nm, which is a critical thickness. Thus, an onset of tetragonal structures associated with the β-Ta phase has been shown in addition to the α-Ta phase with the increasing thickness of the magnetic seed layer. Usually, the thickness of Py is varied in Py/Ta heterostructures for the investigation of ISHE and hence the phase of Ta plays an important role in determining different important parameters like $g_{\uparrow\downarrow}$ and θ_{SH}. An enhanced spin pumping of $g_{\uparrow\downarrow}$ = 10.1 × 10^{18} m^{-2} is observed in Si/Py (t_{Py})/Ta (18) for the (α + β)-Ta phase ($t_{Py} \geq$ 12 nm) as compared to $g_{\uparrow\downarrow}$ = 7.9 × 10^{18} m^{-2} for the α-Ta (t_{Py} < 12 nm) using FMR measurements. Consequently, the spin-to-charge conversion efficiency is found to be higher for the (α + β)-Ta phase (θ_{SH} = −0.15 ± 0.009) than the α-Ta phase (θ_{SH} = −0.10 ± 0.008) by performing ISHE measurements. Our results demonstrate a strong correlation between the phase of Ta and the observed spin-to-charge conversion parameters in Py/Ta heterostructures. Therefore, this work has potential implications in designing efficient ISHE-based spintronic devices *via* seed layer thickness.

Author contributions

CM and AH conceived the idea and coordinated the project. KS and JP prepared the samples. KS performed the structural

characterization and analysed the XRD data. BP and JP performed the FMR based spin pumping and ISHE experiments. KS, BP and JP analysed the FMR and ISHE data. The manuscript was written by KS, AH and CM.

Conflicts of interest

The authors declare no conflict of interest.

Acknowledgements

Notes and references

1 M. I. Dyakonov and V. I. Perel, *Phys. Lett. A*, 1971, **35**, 459–460.

2 M. Johnson and R. H. Silsbee, *Phys. Rev. B: Condens. Matter Mater. Phys.*, 1988, **37**, 5312–5325.

3 J. C. C. Slonczewski, *J. Magn. Magn. Mater.*, 1996, **873**, 865–870.

4 Q. Shao, P. Li, L. Liu, H. Yang, S. Fukami, A. Razavi, H. Wu, F. Freimuth, Y. Mokrousov, M. D. Stiles, S. Emori, A. Hoffmann, J. Akerman, K. Roy, J. Wang, S. Yang, K. Garellob and W. Zhang, *IEEE Trans. Magn.*, 2021, 1–39.

5 D. Sanchez Hazen, S. Auffret, I. Joumard, L. Vila, L. D. Buda-Prejbeanu, R. C. Sousa, L. Prejbeanu and B. Dieny, *Nanoscale*, 2021, **13**, 14096–14109.

6 J. Wang, Q. Huang, P. Shi, K. Zhang, Y. Tian, S. Yan, Y. Chen, G. Liu, S. Kang and L. Mei, *Nanoscale*, 2017, **9**, 16073–16078.

7 G. J. Lim, D. Chua, W. Gan, C. Murapaka and W. S. Lew, *Adv. Electron. Mater.*, 2020, **6**, 1901090.

8 J. E. Hirsch, *Phys. Rev. Lett.*, 1999, **83**, 1834–1837.

9 S. Zhang, *Phys. Rev. Lett.*, 2000, **85**, 393–396.

10 E. I. Rashba, *Phys. E*, 2006, **34**, 31–35.

11 Z. Wang, H. Cheng, K. Shi, Y. Liu, J. Qiao, D. Zhu, W. Cai, X. Zhang, S. Eimer, D. Zhu, J. Zhang, A. Fert and W. Zhao, *Nanoscale*, 2020, **12**, 15246–15251.

12 Z. Yu, J. Chen, L. Zhang, Y. Xing and J. Wang, *Nanoscale*, 2018, **10**, 18728–18733.

13 S. O. Valenzuela and M. Tinkham, *Nature*, 2006, **442**, 176–179.

14 T. Kimura, Y. Otani, T. Sato, S. Takahashi and S. Maekawa, *Phys. Rev. Lett.*, 2007, **98**, 156601.

15 T. Tanaka, H. Kontani, M. Naito, T. Naito, D. S. Hirashima, K. Yamada and J. Inoue, *Phys. Rev. B: Condens. Matter Mater. Phys.*, 2008, **77**, 165117.

16 R. H. Silsbee, A. Janossy and P. Monod, *Phys. Rev. B: Condens. Matter Mater. Phys.*, 1979, **19**, 4382–4399.

17 Y. Tserkovnyak, A. Brataas and G. E. W. Bauer, *Phys. Rev. Lett.*, 2002, **88**, 117601.

18 Y. Tserkovnyak, A. Brataas and G. E. W. Bauer, *Phys. Rev. B: Condens. Matter Mater. Phys.*, 2002, **66**, 224403.

19 A. Brataas, Y. Tserkovnyak, G. E. W. Bauer and B. I. Halperin, *Phys. Rev. B: Condens. Matter Mater. Phys.*, 2002, **66**, 060404.

20 Y. Tserkovnyak, A. Brataas, G. E. W. Bauer and B. I. Halperin, *Rev. Mod. Phys.*, 2005, **77**, 1375–1421.

21 M. B. Jungfleisch, V. Lauer, R. Neb, A. V. Chumak and B. Hillebrands, *Appl. Phys. Lett.*, 2013, **103**(2), 022411.

22 T. K. H. Pham, M. Ribeiro, J. H. Park, N. J. Lee, K. H. Kang, E. Park, V. Q. Nguyen, A. Michel, C. S. Yoon, S. Cho and T. H. Kim, *Sci. Rep.*, 2018, **8**, 13907.

23 R. Bansal, N. Behera, A. Kumar and P. K. Muduli, *Appl. Phys. Lett.*, 2017, **110**(20), 202402.

24 S. N. Panda, S. Majumder, A. Bhattacharyya, S. Dutta, S. Choudhury and A. Barman, *ACS Appl. Mater. Interfaces*, 2021, **13**, 20875–20884.

25 D. Jhajhria, N. Behera, D. K. Pandya and S. Chaudhary, *Phys. Rev. B*, 2019, **99**, 014430.

26 A. Kumar, N. Behera, R. Gupta, S. Husain, H. Stopfel, V. Kapaklis, R. Brucas and P. Svedlindh, *J. Phys. D: Appl. Phys.*, 2020, **53**(35), 355003.

27 V. Vlaminck, J. E. Pearson, S. D. Bader and A. Hoffmann, *Phys. Rev. B: Condens. Matter Mater. Phys.*, 2013, **88**, 064414.

28 L. Liu, C. F. Pai, Y. Li, H. W. Tseng, D. C. Ralph and R. A. Buhrman, *Science*, 2012, **336**, 555–558.

29 E. Sagasta, Y. Omori, S. Vélez, R. Llopis, C. Tollan, A. Chuvilin, L. E. Hueso, M. Gradhand, Y. Otani and F. Casanova, *Phys. Rev. B*, 2018, **98**, 060410.

30 J. Liu, T. Ohkubo, S. Mitani, K. Hono and M. Hayashi, *Appl. Phys. Lett.*, 2015, **107**(23), 232408.

31 H. Gamou, Y. Du, M. Kohda and J. Nitta, *Phys. Rev. B*, 2019, **99**, 184408.

32 A. Kumar, R. Bansal, S. Chaudhary and P. K. Muduli, *Phys. Rev. B*, 2018, **98**, 104403.

33 S. Emori, U. Bauer, S. M. Ahn, E. Martinez and G. S. D. Beach, *Nat. Mater.*, 2013, **12**, 611–616.

34 L. Liu, X. Zhao, W. Liu, Y. Song, X. Zhao and Z. Zhang, *Nanoscale*, 2020, **12**, 12444–12453.

35 A. A. Navid and A. M. Hodge, *Scr. Mater.*, 2010, **63**, 867–870.

36 P. Catania, J. P. Doyle and J. J. Cuomo, *J. Vac. Sci. Technol., A*, 1992, **10**, 3318–3321.

37 A. A. Navid and A. M. Hodge, *Mater. Sci. Eng., A*, 2012, **536**, 49–56.

38 J. J. Colin, G. Abadias, A. Michel and C. Jaouen, *Acta Mater.*, 2017, **126**, 481–493.

39 K. Hieber and E. Lautenbacher, *Thin Solid Films*, 1980, **66**, 191–196.

40 P. Saravanan, J. H. Hsu, C. L. Tsai, A. K. Singh and P. Alagarsamy, *IEEE Trans. Magn.*, 2015, **51**, 2006604.

41 A. Fillon, G. Abadias, A. Michel, C. Jaouen and P. Villechaise, *Phys. Rev. Lett.*, 2010, **104**, 096101.

42 C. Kittel, *Phys. Rev.*, 1948, **73**, 155–161.

43 R. Urban, G. Woltersdorf and B. Heinrich, *Phys. Rev. Lett.*, 2001, **87**, 217204.

44 P. Lubitz, S. F. Cheng and F. J. Rachford, *J. Appl. Phys.*, 2003, **93**, 8283–8285.

45 M. Zwierzycki, Y. Tserkovnyak, P. J. Kelly, A. Brataas and G. E. W. Bauer, *Phys. Rev. B: Condens. Matter Mater. Phys.*, 2005, **71**, 064420.

46 A. Brataas, Y. Tserkovnyak, G. E. W. Bauer and P. J. Kelly, *Spin pumping and spin transfer*, Oxford University Press, 2017, vol. 1.

47 K. Chen and S. Zhang, *Phys. Rev. Lett.*, 2015, **114**, 126602.

48 S. M. Watts, J. Grollier, C. H. Van Der Wal and B. J. Van Wees, *Phys. Rev. Lett.*, 2006, **96**, 077201.

49 E. Šimánek and B. Heinrich, *Phys. Rev. B: Condens. Matter Mater. Phys.*, 2003, **67**, 144418.

50 E. Šimánek, *Phys. Rev. B: Condens. Matter Mater. Phys.*, 2003, **68**, 224403.

51 S. Mizukami, Y. Ando and T. Miyazaki, *Jpn. J. Appl. Phys.*, 2001, **40**, 580.

52 S. Mizukami, Y. Ando and T. Miyazaki, *Phys. Rev. B: Condens. Matter Mater. Phys.*, 2002, **66**, 104413.

53 F. Group, *Handbook of spin transport and magnetism*, 2012.

54 Y. V. Sharvin, *Sov. Phys. JETP*, 1965, **21**, 655.

55 A. Brataas, Y. U. V. Nazarov and G. E. W. Bauer, *Phys. Rev. Lett.*, 2000, **84**, 2481–2484.

56 A. B. Cahaya, A. O. Leon and G. E. W. Bauer, *Phys. Rev. B*, 2017, **96**, 144434.

57 M. Tang, R. Ramaswamy, H. Yang, H. Yang, W. Fan, Z. Shi, S. Zhou and X. Qiu, *Appl. Phys. Lett.*, 2018, **113**, 222406.

58 A. Kumar, R. Sharma, K. I. Ali Khan, C. Murapaka, G. J. Lim, W. S. Lew, S. Chaudhary and P. K. Muduli, *ACS Appl. Electron. Mater.*, 2021, **3**(7), 3139–3146.

59 R. Iguchi and E. Saitoh, *J. Phys. Soc. Jpn.*, 2017, **86**, 53–55.

60 J. M. Shaw, H. T. Nembach and T. J. Silva, *Phys. Rev. B: Condens. Matter Mater. Phys.*, 2012, **85**, 054412.

61 E. Saitoh, M. Ueda, H. Miyajima and G. Tatara, *Appl. Phys. Lett.*, 2006, **88**, 182509.

62 A. Conca, B. Heinz, M. R. Schweizer, S. Keller, E. T. Papaioannou and B. Hillebrands, *Phys. Rev. B*, 2017, **95**, 174426.

63 X. Tao, Q. Liu, B. Miao, R. Yu, Z. Feng, L. Sun, B. You, J. Du, K. Chen, S. Zhang, L. Zhang, Z. Yuan, D. Wu and H. Ding, *Sci. Adv.*, 2018, **4**, eaat1670.

64 Y. Niimi, H. Suzuki, Y. Kawanishi, Y. Omori, T. Valet, A. Fert and Y. Otani, *Phys. Rev. B: Condens. Matter Mater. Phys.*, 2014, **89**, 054401.